IEEE Access
Multidisciplinary | Rapid Review | Open Access Journal

Received October 31, 2017, accepted December 22, 2017, date of publication January 9, 2018,
date of current version February 28, 2018.

Digital Object Identifier 10.1109/ACCESS.2018.2791427

Detection of Glaucoma Using Cup to Disc Ratio From Spectral Domain Optical Coherence Tomography Images

TEHMINA KHALIL[1], M. USMAN AKRAM[2], HINA RAJA[2], AMINA JAMEEL[3], AND IMRAN BASIT[4]

[1]Department of Software Engineering , Bahria University, Islamabad 10250, Pakistan
[2]Department of Computer Engineering, National University of Sciences and Technology, Islamabad 44000, Pakistan
[3]Department of Computer Engineering, Bahria University, Islamabad 10250, Pakistan
[4]Armed Forces Institute of Ophthalmology, Rawalpindi 507101, Pakistan

Corresponding author: Tehmina Khalil (tehmina_khalil08@yahoo.com)

This work was supported by the Higher Education Commission, Pakistan, under the National Research Program for Universities.

ABSTRACT Glaucoma is an asymptomatic neurological disease. It causes damage to optic nerve due to increased fluid pressure within eyes. In the proposed system, cup-to-disc-ratio has been computed considering internal layers of the retina using spectral-domain optical coherence tomography images. In the cup-diameter-calculation process, cup contour has been extracted from inner-limiting-membrane (ILM) layer. The paper introduces a new method to improve the precision of the ILM-layer extraction. It also employs a novel technique to refine contour of an ILM layer. The novel method has outperformed interpolation and Bezier curve fitting in term of outliers' removal and surface refinement. In the disc-diameter-calculation process, the retinal-pigment-epithelium (RPE) layer end points have been used to define disc margin. Prior to RPE-layer extraction, ILM-Layer removal has been done by an innovative strategy to locate and remove ILM-layer. Finally, precise RPE-layer extraction has been done based on the novel thickness-value (T_V) estimation method. Furthermore, a new criterion for cup edges determination, based on the mean value of RPE-layer end points, is proposed. The proposed system has shown a clear precedence over its contemporary systems in terms of accuracy and handling of acute cases. Satisfactory results have been obtained when compared with the clinical results.

INDEX TERMS Optical coherence tomography, computer vision, biomedical informatics, telemedicine.

I. INTRODUCTION

Glaucoma is a chronic and painless ocular disease. It remains unnoticeable in the initial and treatable stage due to slow progression and painless damage to Optic Disc (OD) of the eye [1]. It is an asymptomatic neurological disease which occurs due to increase in fluid pressure within the eyeball [2]. Elevated pressure inside the eye damages the nerve fibers (axons) in Retinal-Nerve-Fiber (RNF) layer [3]. It starts with minor disorders and decay of nerve fibers. These defects are so minor that they usually remain unnoticeable in the initial phases of glaucoma. In the intermediate stage, changes in RNF-layer and slight peripheral vision loss occur with no noticeable symptoms. Glaucoma eventually appears as a disease in its later and final stage with severe peripheral vision loss and ultimately blindness [4].

The absence of warning behavior of glaucoma has been a serious challenge for researchers for centuries. Even in the present, highly medically advanced world, there exists a frightening record of undiagnosed glaucoma patients. In Singapore, around 90% of glaucoma affected people have been unaware of their condition [5], [6]. Almost 50% patients are left undiagnosed in Australia [7]. In the US, approximately 4 million people suffer from this disease and again half of them have been unaware of their disease [8]. The existing pre-diagnosis procedure for glaucoma is invasive, expensive and time-consuming. The Quantitative methods for glaucoma diagnosis can reduce variability and increase precision. Two leading imaging modalities used in glaucoma diagnosis are Funduscopy and Optical-Coherence-Tomography (OCT). Funduscopy is convenient and gives a magnified view of posterior part of the eye. Yet, it can only capture structural changes on the outermost layer of the retina which appear in the last and untreatable stage. There is a dire need to capture internal structural changes introduced by glaucoma in the

initial and treatable stage. Structural changes in retinal layers occur prior to VF loss [1]. The early and timely diagnosis of these changes can prevent blindness as glaucoma can be treated at initial stages [9]. Modern imaging modality such as OCT has the ability to produce objective and reproducible measurements of topographic parameters of retinal layers. It functions as a form of ''Optical biopsy''. It enables imaging retina in a 3-D manner which enables detailed quantification of structural changes [10]. It is capable of generating a cross-sectional view of the retinal layers which is not available in Funduscopy. The cup is the central white portion of OD with no nerve fibers. In glaucoma, the decay of the fiber nerves causes cup size to increase and as a result, the Cup-to-Disc-Ratio (CDR) also increases. CDR is one of the main clinical indicators involved in glaucoma diagnosis [11]. The CDR value less than 0.5 is considered as normal, whereas greater than or equal to 0.5 is considered as glaucomatous. In the initial and intermediate stage of glaucoma, the vertical CDR increases rapidly [12].

Our study has been aimed to develop a reliable and robust automated system to compute vertical CDR from SD-OCT images for more accurate and early diagnosis of glaucoma. The results of proposed system have been compared with the CDR values of fundus images of the same patient to gauge the suitability of imaging modality for early and accurate diagnosis. Calculated CDR values have been also compared with clinical CDR values to analyze concordance with values annotated by medical experts to evaluate the performance of the proposed system.

II. LITERATURE REVIEW

Automated diagnosis of glaucoma using OCT images has been the focus of a broad range of researchers during recent years. Some recent contributions in this evolving area are discussed in the following section.

A. CLINICAL INVESTIGATIONS

In a clinical study, Hrynchak *et al.* [13] have compared CDR values of healthy eyes extracted from visual inspection of OCT images with clinical judgments of CDR values from funduscopy. Clinical judgment has been done through dilated pupil of 20 subjects by two experienced clinicians. Likewise, OCT images for a cup and disc extraction have been analyzed separately by two examiners. The cup edges have been considered as the uppermost points on the surface of optic nerve before the inward inflection. Similarly, the termination points of Retinal-Pigment-Epithelium (RPE) layer have been taken as disc margin. Cup width has been measured at two different points. First, the width has been calculated at a point 1/2 way down both sides and then at a point 1/3 down both sides of cup. Results showed that the CDR values calculated by taking cup width at a point 1/2 way down slope have been closer to CDR values of clinical judgment.

Also in 2005, a study has been conducted to discover the best OCT scanning region for effective and accurate glaucoma diagnosis [14]. 72 subjects have been involved in the analysis. Complete ocular inspection, Visual-Field (VF) testing and OCT scanning of the macula, peripapillary and Optic-Never-Head (ONH) region have been done for each subject on the same visit. The performance of each scanned area has been calculated to discriminate between glaucomatous and healthy eyes by using the Area-under-Receiver-Operating-Characteristic-Curve (AROCs). The rim area ONH parameter showed the largest AROCs with 0.97. Results showed that ONH parameters have the best discrimination capabilities to differentiate between glaucomatous and healthy subjects.

The topographic measurements of OD of normal Indian eyes of 150 subjects have been studied in 2006 [15]. Automatic analysis of images have been done by using a specific software. The analysis showed that the OD vertical diameter has been larger than the horizontal diameter in 88% subjects. Similarly, rim vertical width has been found to be significantly larger than horizontal rim width. Likewise, the horizontal cup diameter has been found to be larger than the vertical cup diameter. The mean CDR found to be 0.33 ± 0.15. Result also revealed no significant difference between OD properties of male and female eyes. Likewise, a cross-sectional study has been conducted by Leung *et al.* [16] to demonstrate the importance of the level of the reference plane and its impact on the measurement of ONH values. RFN-layer thickness and ONH parameters of 101 subjects have been calculated at 95,150 and 205 micrometer (μm) above the level of RPE-layer. Statistical analysis of each calculated parameter with respective visual field mean deviation value has been done using linear regression. Results showed the values measured at 150μm above RPE-layer yielded the best results for early glaucoma detection. It has been found that the level of reference plane has a great impact on the values of ONH measurement. It has been recommended that the level of reference plane should remain constant in the successive analysis. A recent study in 2014 has been conducted to compare the VF defects and OCT parameters [17]. It examines the relationship between the type of OD impairment and effectiveness of OCT parameters for glaucoma diagnosis. A total of 298 subjects have been used in the analysis. The subjects have been divided into four groups based on OD damage. Focal-Ischemic (FI) group referred subjects with focal loss of OD area, Myopic (MY) denoted to titled OD, Senile-Sclerotic (SS) represented OD with shallow cupping and Generalized-Enlargements (GE) indicated enlarged cup OD. Superior-Inferior (S-I) differences, OD Parameters, RNF-layer and Ganglion-Cell-Inner-Plexiform-layer (GCIPL) thickness have been calculated. Results established that S-I differences have been greater in GE group while the SS group has the largest rim area. The CDR of the GE group has been found to be larger than the MY group. The GCIPL thickness of the GE group has been established as larger than the FI group. Overall result showed variation in OCT parameter values of four groups due to different OD forms. Table 1 summarizes the investigations and findings of above mentioned clinical research studies.

TABLE 1. Clinical investigation summary.

Author	Investigation	Subjects Involved	Findings
P. Hrynchak et al. (2004) [13]	Best point to calculate cup diameter for CDR	20	Best point to compute CDR was discovered ½ way down cup depth
G. Wollstein et al. (2005) [14]	Best OCT scanning region for glaucoma detection	72	OD Rim was detected as best OCT scanning region for glaucoma detection
S. Dacosta et al. (2006) [15]	Topographic OD analysis	150	OD vertical diameter found to greater than horizontal diameter
C. Leung et al. (2005) [16]	Best reference plane position for glaucoma diagnosis	101	150 μm above RPE layer found to be best reference plane position for glaucoma detection
H. Shin et al. (2014) [17]	Effect of OD damage on OCT parameter values	298	OD damage cause significant variation in OCT parameter values

B. AUTOMATED DIAGNOSIS

Wu *et al.* [18] proposed an automated CDR calculation algorithm using OCT images in 2015. It consists of two main phases. The disc margins have been located in the first phase, whereas, a patch searching algorithm using Support-Vector-Machine (SVM) has been deployed in the second phase. Disc margin localization included removal of speckle noise using bilateral filters and image resampling in x-axis direction for better results. The outer boundary of RPE-layer has been segmented using 3-D graph search approach. The points with maximum curvature on RPE-layer have been taken as Neural-Canal-Opening (NCO). In the second phase, the most likely patch has been extracted by SVM classifier using local binary patterns and histogram of gradient features. Next, patches with the highest probability closest to NCO candidates have been selected by using a searching method. The Cup border has been calculated on the basis of NCO location and Inner-Limiting-Membrane (ILM) layer boundary. Finally, the CDR value has been calculated. The system has been evaluated on OCT images of 17 patients. Results showed high segmentation accuracy and low CDR evaluation error when compared with manually calculated CDR values.

Similarly, another automated CDR calculation algorithm has been proposed in 2013 [19]. It used bilateral filtering to remove speckle noise. The Otsu's thresholding has been applied to highlight RFN-layer. Open operations have been applied to remove isolated speckles. ILM-layer has been detached by removing all topmost pixels with similar neighbors from the image. The RPE-layer has been extracted by taking the brightest area of each column. Image flattering has been done by ignoring all points beyond a specified distance. These flattened binary images have been used to locate RPE-layer break points. These points have been further altered by constraint based on RPE and ILM layer. The distance between the RPE-layer edges defined the disc diameter. The cup diameter has been extracted at a distance around 150μm from the optic disc edges. The result showed that the proposed system was able to detect glaucoma cases to some extent. In 2015, Nithya and Venkateswaran [20] used both OCT and fundus images of same subjects for glaucoma diagnosis. The target has been to evaluate the effectiveness of both imaging modality and corresponding algorithm. In fundus images, the CDR has been calculated using different segmentations algorithms for both cup and disc segmentation. In OCT, first RGB color space has been transformed to LAB space. Then the L channel has been used for the detection of RPE and RNF layer segmentation using second order derivatives. Two horizontal and vertical lines have been marked with reference to the middle of the image. The two points intersecting on RPE-layer have been considered as cup diameter. In the same way, the intersection points on RNF-layer have been taken as disc diameter. The CDR has been finally calculated using both the diameters. Results showed the significant superior performance of OCT image analysis.

Likewise, in the same year, Babu *et al.* [21] involved both fundus and OCT images in the automated glaucoma detection. Two structural features, CDR and ISNT ratio have been used for fundus image classification using Back-Probation-Neural_Network (BPN) and SVM. In OCT image classification, primarily, the CDR has been computed using morphological operations to detect Retinal-Vitreal (RV) and Retinal-Choroid (RC) boundaries. Next, these boundaries have been used to calculate the edges of cup and disc. CDR calculation has been further improved by segmenting RV using wavelet transform and RC has been extracted using multilevel thresholding. RC and RV boundaries have been made smooth using Bezier curve fitting. Likewise; retinal thickness has been calculated by counting white pixels in the 2nd and 3rd quadrant of a binary image obtained by multilevel thresholding. The RV boundary has been additionally used to calculate cup depth. Above mentioned three OCT image features have been used for classification using BPN and SVM. 150 OCT images have been used for evaluation of the system. Results showed better performance of fundus images in both classifiers. The OCT module attained 93.83% accuracy.

In 2012 an automated system has been developed by utilizing RV-layer boundary and region of RC in CDR computation [22]. The RV-layer boundary has been segmented using wavelet transform on red plane image and RC region has been computed using multilevel thresholding. Bezier curve has been applied to smooth boundaries of RC and RV layer. A total of 125 images have been used for the evaluation of the system and attained 92% accuracy. Table 2 shows

TABLE 2. Retinal layers used in glaucoma detection using OCT images.

Author	Disc Analysis Layer	Cup Analysis Layer	Dataset	Accuracy
M. Wu et al.(2015) [18]	RPE-layer	ILM-layer	17	---
Y. Wang et al.(2013) [19]	RPE-layer	ILM-layer	---	---
R. Nithya et al.(2015) [20]	RNF-layer	RPE-layer	---	---
T. Ganesh Babu et al.(2015) [21]	RC-layer	RV-layer	150	93.83%
T. Babu et al.(2012) [22]	RC-layer	RV-layer	125	92%

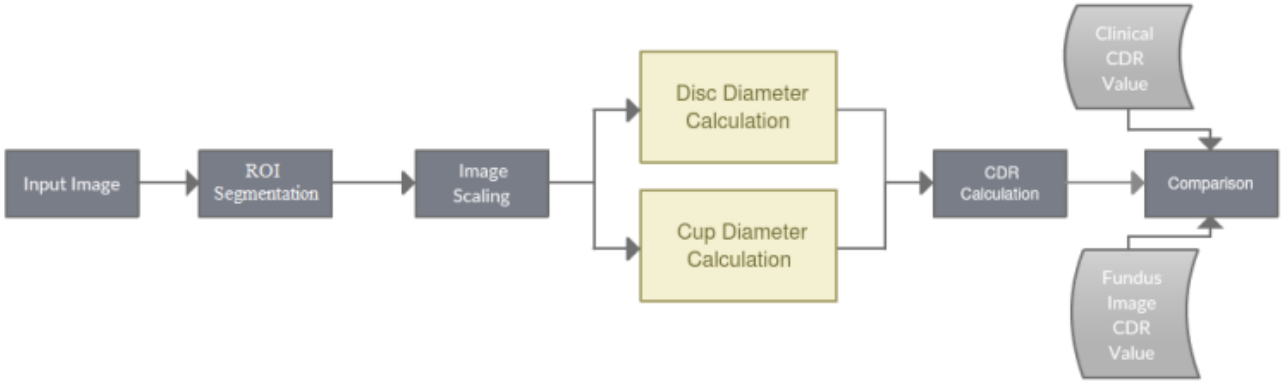

FIGURE 1. Overview/architecture of proposed system.

different retinal layers used for the disc and cup analysis using OCT images in glaucoma detection.The analysis of existing systems revealed that automated glaucoma detection using the OCT images still have a lot of room for improvement. The retinal layers have not been properly explored to extract the CDR for glaucoma detection. Moreover, there is no standard dataset available for the OCT image analysis for glaucoma.

III. PROPOSED METHOD

The figure 1 shows an overview of the proposed methodology. Initially, the input SD-OCT image has been preprocessed before the cup and disc diameter calculation. Then, the CDR value has been derived from the calculated cup and disc diameter. Finally, the analysis of concordance of the results has been done with CDR values annotated by ophthalmologists and already calculated CDR values using fundus images of same patients.

The preprocessing stage further comprises of two steps. It starts with the segmentation of region of interest (ROI) by placing cup exactly in the center with almost equal retinal layers on both sides [23]. In the next step, the spatial resolution has been improved using bilinear interpolation technique for more accurate results [24]. In the proposed system, the green channel of the processed image has been used for ILM and RPE layers extraction. The ILM and RPE are the two most prominent layers in the SD OCT image. Figure 2 highlights both layers.

A. THRESHOLDING METHODOLOGY

In the proposed system, we have computed a set of threshold values based on input image gray level distribution by

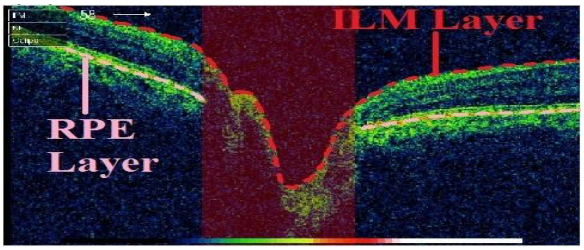

FIGURE 2. Retinal layers.

using multi-level Otsu algorithm [25]. The threshold value, which minimizes the input image intra-class variance has been selected. The Otsu algorithm is then recursively applied to each image region until the desired number of threshold n_t is obtained. In the proposed system, we have computed six-level threshold values by taking $n_t = 6$ and selected different levels to segment disc and cup from the input image.

B. CUP DIAMETER CALCULATION (CDC) PROCESS

The Gray-Scale Image (GSI) of green channel has been used in the CDC process for ILM-layer extraction after the removal of noise. Primarily, the ILM-layer filtration process has been applied to boost the ILM-layer on GSI. Then, the thresholding has been applied to segment retinal layers from the scaled image. The top profile of segmented retinal layers has been computed to extract the ILM-layer. Then, the ILM-layer Top Surface (TS_{ILM}) has been refined using a set of proposed novel techniques. Finally, the cup edges have been located on the refined top profile on the basis of the end point of RPE-layer. The complete process of cup diameter calculation is elaborated in figure 3.

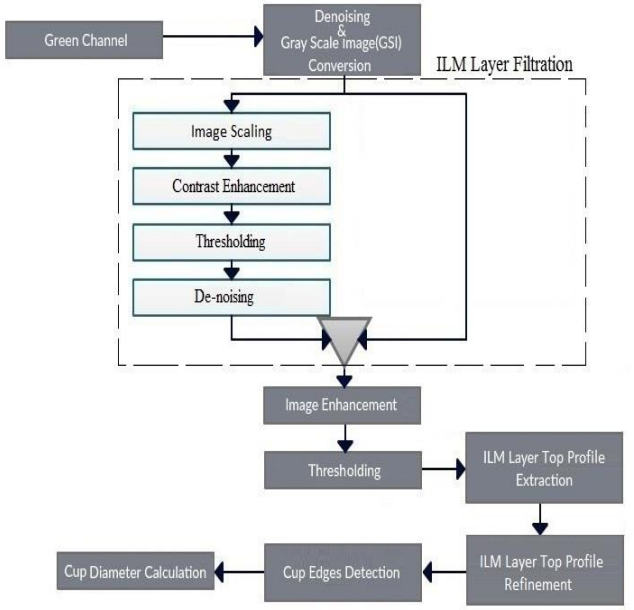

FIGURE 3. CDC process flow chart.

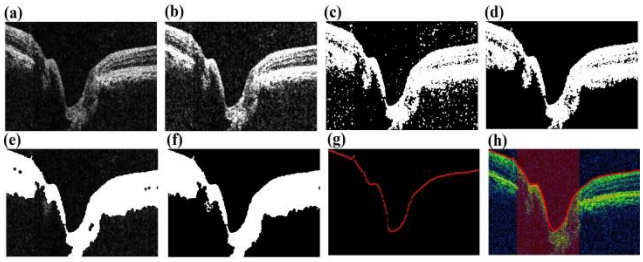

FIGURE 4. TS_{ILM} Extraction & Refinement, (a) GSI image, (b) ILM-layer enhancement by arithmetic operation (2*GSI) & contrast enhancement, (c) thresholding, (d) de-noising, (e) the images shown in (a) & (d) are merged after morphological operations to get enhanced ILM-layer, (f) 'ILM binary image' after thresholding & noise removal, (g) extracted in red color, (h) refined TS_{ILM} using proposed methods.

1) DE-NOISING AND GRAY SCALE CONVERSION

The OCT images encounter speckle noise due to the coherent property of the image construction process. This noise limits the contrast, which impedes the analysis of the structural feature. Therefore, it was necessary to regularize background by removing the speckle noise before extracting topographic measurements of the retina. The wiener filter have been effectively used to reduce speckle noise by means of 2-D adaptive noise removal filtration [26]. It filters the image using neighborhoods of size m-by-n to compute the local image mean and standard deviation [27]. In the case of the ILM-layer segmentation in the CDC process, 15 × 15 neighborhoods have been used to filter green channel by means of wiener filter. The grayscale conversion of the image has been done after the noise removal [28].

2) ILM-LAYER FILTRATION

The ILM-layer extraction was one of the most vital and sensitive parts in the CDC process. The accuracy of the cup diameter is directly proportional to the accuracy of the ILM-layer contour extraction. A slight deviation or variation can lead to an inaccurate CDR calculation. In this research, a unique method has been proposed to facilitate accurate and comprehensive filtration of the ILM-layer, which makes it more conspicuous than the background. This method can effectively highlight almost the entire portion including poor visualization portions of the ILM-layer. The ILM-layer filtration process has two main parts. In the first part, the GSI (figure 4 (a)) image has been split into another GSI image i.e. GSI-1 (figure 4 (b)). Then, GSI-1 has been enhanced to lurid all major portions including reduced visualization regions using a set of image enhancement techniques. In the second part, the fusion of both GSI images has been done to synthesis the boosted ILM-layer with the initial GSI image.

In the pre-processing of GSI-1, initially the GSI image has been scaled by a factor of 2 to enhance the ILM-layer. This operation doubled the value of each pixel and made brighter part extremely dazzling. In this way, all portions including the poor visualization portions of the ILM-layer became equally bright. The contrast of the ILM-layer has been further adjusted so that 1% of the data is saturated at low and high intensities [29].

After the image enhancement, level-3 threshold value has been used to threshold resultant image to slice the enhanced ILM-layer. The figure 4 (c) shows binary image after thresholding. Moreover, any object having an area smaller than a pre-defined size P has been removed [30]. The value of P has been empirically derived from images generated through the scaling process. The average thickness of retinal layers of given data set has been used to define the value of P. This operation only retained the large connected portions of the ILM-layer and discarded any smaller disconnected portion including speckle noise. Figure 4 (d) shows the extracted ILM-layer from GSI-1. When the 2*GSI operation has been applied on the images with poor visualization of retinal layers, it has also increased the speckle noise. The removing of enhanced speckle noise also eradicated some portions of the ILM-layer. This problem has been tackled by merging both the GSI and GSI-1 images. The resultant image only improved the ILM-layer and did not increase the speckle noise. In figure 4 (e), the enhanced ILM-layer can be seen after the merging of both GSI images.

Figure 5 demonstrates the effectiveness of the proposed strategy for the ILM-layer enhancement. It compares results of the same input image in the CDC process with and without the proposed ILM-layer filtration method by following the same pre-processing steps. Scenario 1 in figure 5 shows TS_{ILM} extraction following all steps in the CDC process except the proposed ILM-layer filtration process. In figure 5 (d-1), it could be observed that the proposed CDC process failed to detect the accurate TS_{ILM}. This error occurred due to some less visible portion of the retinal layers. Likewise, in scenario 2 the same input image has been used to

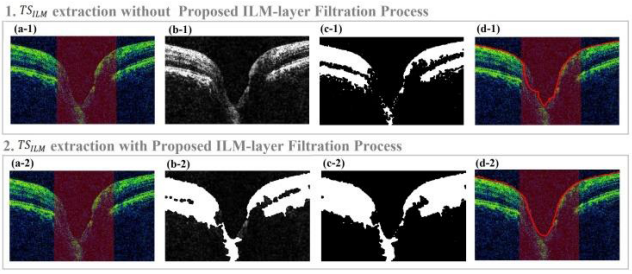

FIGURE 5. Comparison of TS_{ILM} calculation using proposed ILM-layer filtration process VS TS_{ILM} calculation without proposed ILM-layer filtration process, (a-1) input image, (b-1) ILM-layer enhancement applying 2∗GSI arithmetic operation, (c-1) binary image after thresholding, (d-1) extracted TS_{ILM} without using proposed ILM-layer filtration process, (a-2) input image, (b-2) enhanced ILM-layer using proposed filtration process, (c-2) binary image after thresholding, (d-2) extracted TS_{ILM} using proposed ILM-layer filtration process.

calculate TS_{ILM} using the proposed ILM-layer filtration process following all pre-processing steps of the CDC process. Figure 5 (d-2) shows a substantial improvement and accuracy in TS_{ILM} calculation using the proposed ILM-layer filtration process.

3) IMAGE ENHANCEMENT

After the ILM-layer filtration, the morphological closing has been applied to fuse portions of ILM-layer extracted in GSI and GSI-1 [31]. In this way, a solid and fully merged ILM-layer has been obtained. Gaps and holes left in ILM-layer were filled using morphological operation by means of 6-connected neighbours to fill any holes on the resultant image. A hole is an area of dark pixels surrounded by white pixels [32]. Figure 4 (f) shows ILM-layer after application of morphological operations in order to fuse the extracted ILM-layer portion from both GSI and GSI-1.

4) THRESHOLDING

The level-4 threshold value has been used to segment ILM-layer in the CDC process. Figure 4 (f) shows 'ILM binary image' after thresholding and noise removal. The binary image holds several small noisy white objects after the thresholding. These noisy objects have been removed by eliminating any object smaller than a pre-defined size P.

5) ILM LAYER TOP SURFACE (TS_{ILM}) EXTRACTION

The TS_{ILM} calculation from extracted ILM-layer has been done to segment TS_{ILM} and cup contour. The TS_{ILM} has been extracted by identifying row index of first ON pixel on top of each column in 'ILM binary image' (Figure 4 (f)) [33].

6) OUTLIERS REMOVAL AND INTERPOLATION

The outliers are extreme observation points that are detached and grossly inconsistent with the remaining data. They do not conform to the overall model of the data. They normally occur due to variability in the measurements or experimental error. It is important to exclude outliers; otherwise, they may mislead the interpretation of gathered data [34]. In TS_{ILM}, several outliers have been encountered after the thresholding. Figure 6 (a) shows an exemplary 'ILM binary image' generated after the thresholding step in the CDC process. The segmented ILM-layer has almost three missing portions. Similarly, it can be seen that it has several outliers and consecutive missing points. These missing regions have been highlighted with the yellow lines while the outliers have been pointed using blue, lines. The purple boxes shows roughness generated due to presence of speckle noise at the contour of ILM-layer. The figure 7 shows a simulation of the proposed outliers' removal method. Figure 7 (a-1) shows outliers encircled in blue. Figure 7 (b-1) shows the adapted strategy to reallocate best-fit position by considering a set of left and right ON neighbours. Only four neighbouring points ($N = 4$) on each side and minimum acceptable distance of 1 ($d = 1$) have been used for simulation simplification. On the close analysis of figure 7 (b-1), four neighbouring points on each side of the outlier can be observed. These are highlighted with rectangle/circles of the same colour like the newly allocated position of an outlier. The dull gray coloured point enclosed in a square of some colour shows a removed outlier. The colour of the square enclosing removed gray colour outlier indicates the colour assigned to the newly allocated position of an outlier.

In the proposed system, 70 ON neighbouring points have been considered on each side of the outlier i.e. $N = 70$. Similarly, the maximum acceptable distance d between points has been set as 50 i.e. $d = 50$. Any point with a distance greater than d from its previous point will be removed and reallocated to a new position considering N neighbouring pixels on both sides. In the proposed system, the region of interest was mainly central portions of TS_{ILM}. Therefore, we have ignored the extreme left and right points based on the value of N. The figure 6 (b) shows extracted TS_{ILM} with outliers encircled in blue color. Similarly, figure 6 (c) shows TS_{ILM} after outliers removal by mean of the proposed method. The reallocated points are again shown in blue color.

The method used in the proposed outliers removal and reallocations involves following steps.

The TS_{ILM} has been scanned for missing points after the outliers removal. A missing point is generated if an ON pixel is absent in any column. These missing points need to be filled for accurate cup diameter calculation. The proposed method for interpolation considers both immediate left and right set of neighbouring ON pixels for the prediction of missing point. Since TS_{ILM} holds row position of first ON pixel in each column, therefore, the mean of the set of right and left ON pixels value (row position) has been calculated to predict missing point on TS_{ILM}.

The proposed strategy provided excellent results in predicting the values for missing points in negative and positive as well as in the flat slope of the line In case of consecutive missing points, the system will find immediate next ON pixels after group of missing points and considers them as set

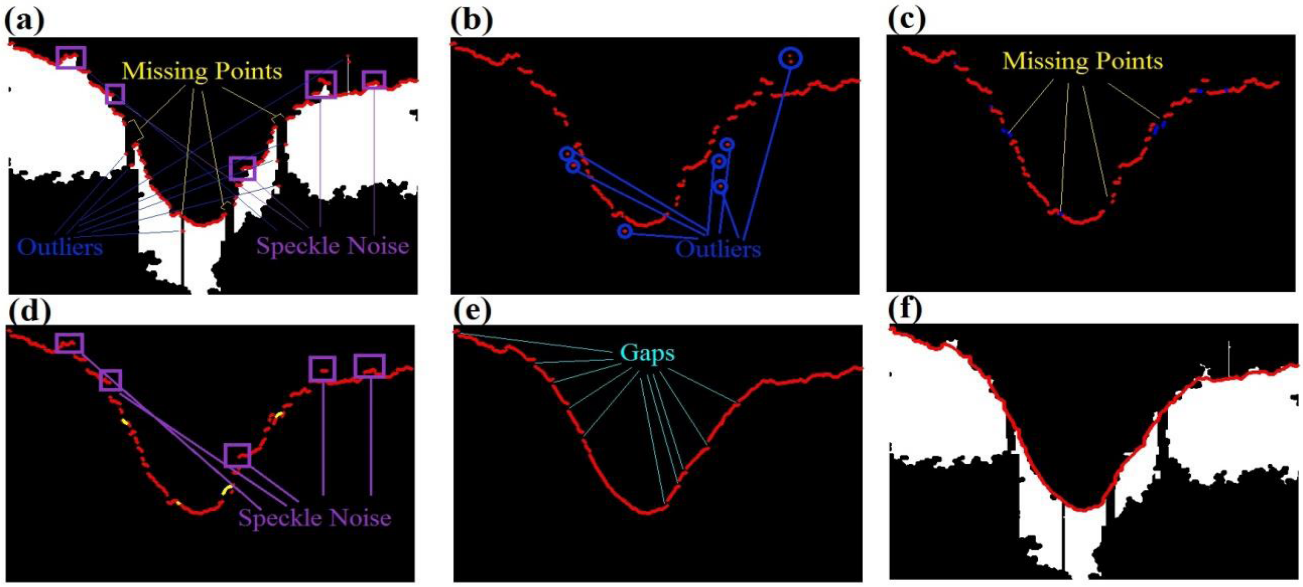

FIGURE 6. TS_{ILM} extraction & refinement, (a) exemplary 'ILM binary image', (b) extracted TS_{ILM} with missing points and outliers, (c) TS_{ILM} outliers removal, reallocated points are shown in blue color, (d) TS_{ILM} interpolation. Predicted points are shown in yellow, (e) TS_{ILM} smoothing and speckle noise removal. Green lines point out gaps, (f) extracted TS_{ILM} after filling gaps is displayed in red color on the input 'TSimg' binary image.

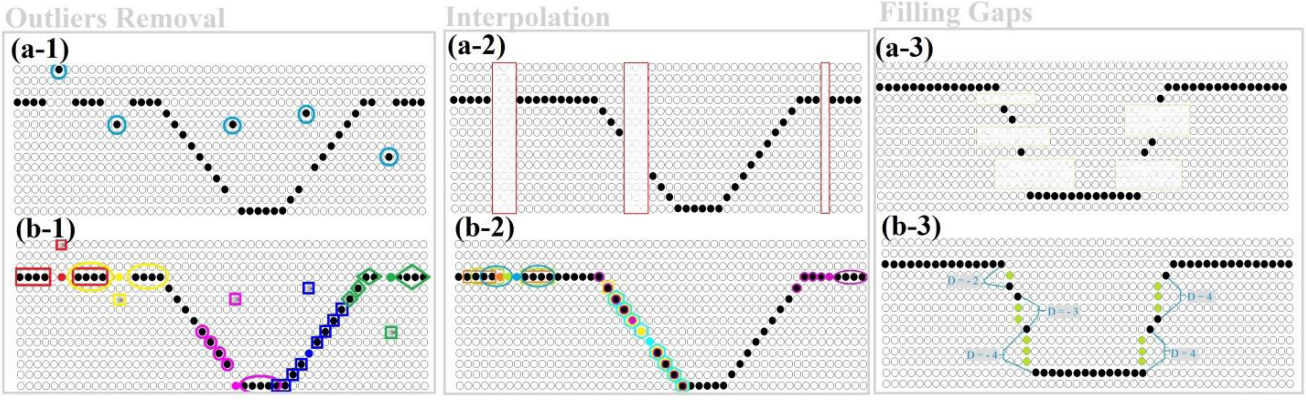

FIGURE 7. TS_{ILM} refinement method simulation, (a-1) TS_{ILM} with some outliers highlighted in blue squares, (b-1) the proposed strategy to remove outliers, (a-2) TS_{ILM} with highlighted missing points, (b-2) the proposed strategy to fill missing points, (a-3) TS_{ILM} with highlighted gaps, (b-3) the proposed strategy to fill gaps.

of Right-Neighbouring pixels for prediction. Figure 7 shows a simulation of the proposed interpolation method. For simulation simplification only 4 left and 4 right neighboring ON pixels have been considered. Figure 7 (a-2) shows TS_{ILM} with consecutive missing points. Figure 7 (b-2) illustrates the strategy used for interpolation. It can be observed that in case of successive missing points, each new predicted value serves as a member of Left-Neighbouring pixels in the prediction of next missing point. In this way, the proposed method has predicted the most appropriate values for missing points in positive, negative and flat slope portions i.e. the flat slope will remain flat. Similarly, there is a proper stepwise increment in each predicted value in negative and positive slopes. The figure 6 (c) shows missing points highlighted with yellow lines. on TS_{ILM} after oultiers removal In proposed system, 70 left and 70 right ON pixels have been considered to predict a missing point. The figure 6 (d) shows TS_{ILM} after interpolation using the proposed method. The interpolated points are again shown in the yellow colour.

7) SMOOTHING

The TS_{ILM} has been once again scanned for distant points after the removal of outliers and interpolation which may occur due to the presence of speckle noise at the boundary of the ILM-layer. The distant points (setting $d = 5$) have been reallocated to the new positions based on averaging method of the set of left and right points ($N = 70$) in the TS_{ILM}. This scan has levelled the boundaries and further suppressed

Algorithm 1 TS_{ILM} Outliers Removal

Step 1	START
Step 2	Initialize d to 50
Step 3	For each element in TS_{ILM} (for i = N + 1 to S − N, where S is size of TS_{ILM} and N specifies the number of the set of neighboring points)
Step 4	Calculate distance D with the previous point $D \leftarrow abs(TS_{ILM}(i) - TS_{ILM}(i-1))$
Step 5	IF D > d ▪ $M_R \leftarrow \frac{1}{N}\sum_{n=1}^{N} TS_{ILM}(i+n))$ ▪ $M_L \leftarrow \frac{1}{N}\sum_{n=1}^{N} TS_{ILM}(i-n))$ ▪ $M \leftarrow Round(\frac{1}{2}(M_R + M_L))$ ▪ Set $TS_{ILM}(i)$ to M
Step 6	END IF
Step 7	STOP

the outliers on boundary of the ILM-layer generated due to the speckle noise. Figure 6 (e) shows smooth TS_{ILM} after removing any remaining outliers on the contour of the ILM-layer.

8) FILLING GAPS

A gap is generated due to blank rows between two consecutive points in TS_{ILM}. Figure 6 (e) shows a fully interpolated and outliers free image. Multiple gaps could be observed in the figure despite interpolation. In order to fill gaps, the TS_{ILM} has been examined row-wise for blank rows, whereas, in interpolation the TS_{ILM} has been examined column-wise for missing columns. The filling of gaps to make TS_{ILM} a solid line is one of the prime requirements to enable examination of the cup diameter exactly at desired locations for an accurate CDR calculation. The TS_{ILM} keeps row position of first ON pixel in each column. Therefore, this information has been effectively used to detect the number of blank rows in-between two consecutive points. A difference of each point from its immediate right neighbour has been calculated in order to identify the gap between the points. If the difference is greater than 1, then it indicates the gap between two consecutive points. The value of difference also points out the number of missing rows between two points. Figure 7 (a-3) shows gaps on TS_{ILM} after outliers removal and interpolation. The figure 7 (b-3) shows the strategy adopted to fill the blank rows. A fully solid ILM-layer contour with filled gaps using the proposed method has been shown in figure 6 (f). The proposed method used to find and fill gaps in TS_{ILM} involves two main parts. In first part, the TS_{ILM} after interpolation and outliers removal has been drawn on empty black image 'TSimg' of the same size like input image. In next part, gaps between TS_{ILM} have been identified and filling of gaps has been done on TSimg. The algorithm 2 shows the steps involved in the filling gaps method.

The accuracy of the proposed method used for the ILM-layer contour extraction and refinement can be visualized in figure 6 (f). There is an obvious improvement, smoothness, and accuracy in the refined ILM-layer contour as compared to the initially extracted ILM-layer contour shown in figure 6 (b).

Algorithm 2 TS_{ILM} TS_{ILM} Filling Gaps

Step 1	START
Step 2	For each element in TS_{ILM} (for i = 1 to S, where S is size of $TS_{ILM}TS_{ILM}$)
Step 3	Calculate Gap between rows $G \leftarrow TS_{ILM}(i) - TS_{ILM}(i+1)$
Step 4	IF G < −1 THEN ▪ Set row r ← $TS_{ILM}(i)$ ▪ WHILE r < $TS_{ILM}(i+1)$ • Set TSimg ((r + 1) , i) to 1 • Move to next row by increment in r by 1 ▪ END WHILE
Step 5	ELSE IF G > 1 ▪ Set row r ← $TS_{ILM}(i)$ ▪ WHILE r > $TS_{ILM}(i+1)$ • Set TSimg ((r + 1) , i) to 1 • Move to next row by decrement in r by 1 ▪ END WHILE
Step 6	END IF
Step 7	END

9) COMPARISON OF PROPOSED CONTOUR REFINEMENT WITH EXISTING TECHNIQUES

The curve surface construction based on the specified set of control points can be done using the interpolation and Bezier curve fitting techniques [35]. The figure 8 (a) shows the construction of surface by using the interpolation technique. It can be seen that interpolation can simply seek a surface that contains all the control points. It is unable to handle both the outliers and roughness/deviation on the surface due to the speckle noise. A strong deviation in extracted contour can be seen in the figure 8 (a). Similarly, figure 8 (b) demonstrates the surface constructed using the Bezier curve fitting technique. It gives an approximation curve that passes through the given control points. It can be observed that Bezier curve can handle the outliers to some extent. However, it fails to detect the multiple consecutive outliers and consequently a strong deviation occurs in the surface construction. Besides, it can be seen that Bezier curve fails to minimize roughness/deviation caused by the speckle noise and cannot smooth the surface. Whereas, in figure 8 (c) it can be seen that the proposed method is able to efficiently detect the outliers and reallocate them to the best possible position considering the overall trend of the control points. It effectively handles the roughness generated due to the speckle noise and is able to smooth the contour.

The performance regarding the computational cost of the above mentioned curve surface construction techniques can

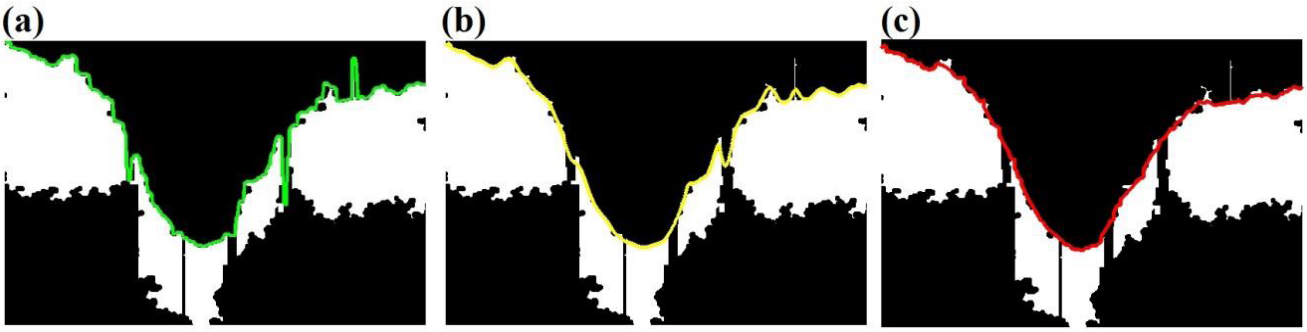

FIGURE 8. Comparison of Proposed Contour Refinement method with existing techniques, (a) surface construction using interpolation technique, (b) surface construction using Bezier curve fitting, (c) surface construction using proposed method.

TABLE 3. Computational time comparison.

Technique	Control Points	Computational Time	System Specification
Interpolation	1645	0.016 Seconds	Operating System: Windows 10 Enterprise Processor : Intel(R) Core(TM) 2.40GHz RAM: 4096MB
Bezier Curve	1645	16.251 Seconds	
Proposed Method	1645	0.031 Seconds	

be analysed in table 3. It can be observed that the proposed method is almost 500 times faster than the Bezier curve. It is taking a computational time of 0.031 second which is almost equivalent to the computational time of the interpolation technique. In this way, the proposed method is able to generate better results in respect of outliers removal and computational cost as compared to the Bezier curve. It is equivalent to the interpolation in terms of the computational cost, which is the simplest method for curve surface construction. Nonetheless, it is giving much improved results than Bezier curve in terms of curve surface refinement and outliers removal.

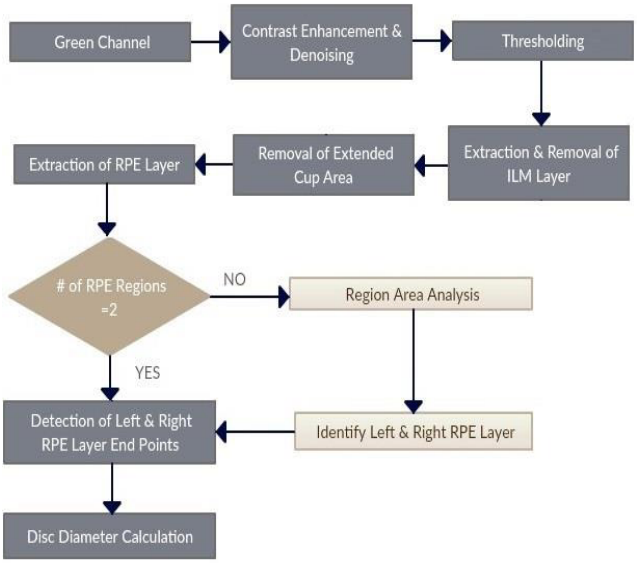

FIGURE 9. DDC process flow diagram.

C. DISC DIAMETER CALCULATION (DDC) PROCESS

In the DDC process, the target has been to segment the RPE-layer and use end points of the RPE-layer to calculate the disc margin. Figure 9 depicts the whole methodology applied in the DDC process.

1) CONTRAST ENHANCEMENT & DE-NOISING

Green channel of the scaled image has been again used in the DDC process. The speckle noise has been removed using wiener filter using 10×10 neighbourhoods of pixels. The numbers of neighbourhood pixels involved in the noise removal have been minimized in the DDC process to keep both the layers isolated without merging. After the noise removal, the image has been converted into the grayscale image. The contrast of grayscale image has been adjusted for better visualization of the retinal layers. Next, morphological closing has been applied on enhanced grayscale image to merge together all small parts of the ILM and RPE layers. This operation will also isolate layers from each other. The remaining holes left in both layers after the morphological closing have been filled by using the morphological operation. Figure 10 (a) shows the ILM and RPE layers after filling of gaps and holes.

2) THRESHOLDING

The level-5 threshold value has been used to segment the retinal layers in the DDC process. The thresholding has been applied to Figure 10 (a) and resultant binary image after removing any area smaller than a pre-defined size P has been shown in Figure 10 (b).

3) ILM-LAYER EXTRACTION & REMOVAL

In order to accurately segment the RPE-layer, it has been required to detect and remove the ILM-layer before the extraction of the RPE-layer. The ILM-layer extraction and removal are one of the most challenging activities in layer segmentation in the DDC process. The morphological operation caused the ILM and RPE layer to get connected at some points. In figure 10 (b), it can be seen that both layers are connected after performing morphological operations. In this

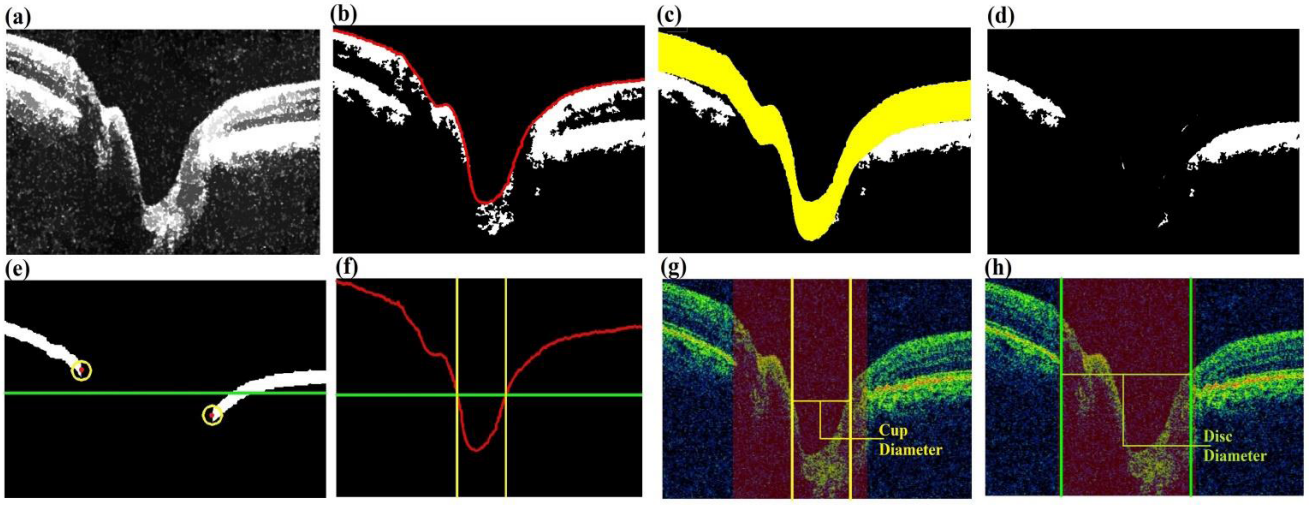

FIGURE 10. RPE layer end points extraction and CDR computation, (a) green channel after noise removal and morphological operations, (b) binary image after thresholding and noise removal. Red line shows TS_{ILM} extracted during CDC Process, (c) yellow portion highlights estimated ILM-layer to be removed using proposed method, (d) survived bottom layer after ILM-layer removal, (e) yellow circles indicate extracted RPE-layer end points. Green line shows mean value of RPE-layer end points, (f) yellow lines show cup edges detected on TSimg based on mean value of RPE-layer end points, (g) yellow horizontal line shows calculated cup diameter, (h) green vertical lines represent disc edges calculated on the base of RPE-layer end points. Horizontal green line shows calculated disc diameter.

way, an attempt to remove the ILM-layer based on the connected component also removes the RPE-layer. Therefore, an innovative strategy has been adopted to remove only the ILM-layer.

In the previous CDC process, the focus remained exclusively on the extraction of ILM-layer without fear of merging it with the RPE-layer. Whereas in current DDC process, care has been taken while applying thresholding and morphological operations in order to keep the layers isolated without merging. However, on the other hand, these operations have also triggered loss of some portions of the ILM-layer causing difficulty in the detection and removal of the ILM-layer. Likewise, there has been extremely poor visualization of the ILM layer in some images and it was impossible to isolate and extract the ILM-layer in the DDC process. Therefore, an innovative method has been adopted to deal with these issues for the successful segmentation of the ILM-layer even with the poor visualization of the ILM-layer.

According to clinical investigations, the quantitative measure of thickness profile of six retinal layers on the top of the RPE-layer in a normal healthy subject is 200 micron on SD-OCT images [36]. The standard SD-OCT image has an axial resolution of 3 micrometer/pixel. Since we have scaled images and enlarged them 3 times than their original size; therefore, we have used the ILM-layer Thickness-Value $TK_{ILM} = 200$ pixels to remove maximum layers on the top of the RPE-layer.

The proposed method used to detect and remove the ILM-layer has two main parts. In the first part, a portion of ILM-layers has been calculated using TS_{ILM} extracted in the CDC process and the predefined value of TK_{ILM} TK_{ILM}. In the second part, the calculated portion of the ILM-layer has been removed from processed binary image 'img' in the DDC process. Figure 10 (b) shows TS_{ILM} calculated in the CDC process, plotted in red color on 'img'. The yellow highlighted portion in figure 10 (c) shows a portion of the ILM-layer to be removed using the proposed method. Figure 10 (d) shows 'img' after removal of the ILM-layer.

4) REMOVAL OF EXTENDED CUP AREAS

The Extended-Cup-Areas (ECA) are those portions of the cup that may survive after the ILM-layer removal. It was important to find and remove ECA before the RPE-layer extraction because in some some cases the survived ECA have found to be as large as the RPE-layer portions. These large portions lead to inaccurate segmentations of the RPE-layer. In the proposed system, the ECA were removed by marking certain portion of 'img' as ECA holder portions. Any object on these specific locations has been considered as ECA and has been removed.When the input image has been cropped, the cup has always been placed in the center with equal retinal layers on both sides. Therefore, any object found at the exact middle of the image has been considered as ECA. Similarly, the retinal layers are always at a certain distance from the bottom of the image due to the presence of the cup. A specific portion at the bottom of the image has also been considered as ECA holder portion. Therefore, in the ECA holder portion no part of the retinal layer can occur except ECA. The proposed method for the ECA removal consists of two main parts. First, a seed point X_{seed} has been identified by searching ECA at specified portions of 'img'. Secondly, the X_{seed} has been used to find all the connected components using 8-point neighborhood [37], [38]. All connected components forming ECA have been removed from 'img' in the proposed method.

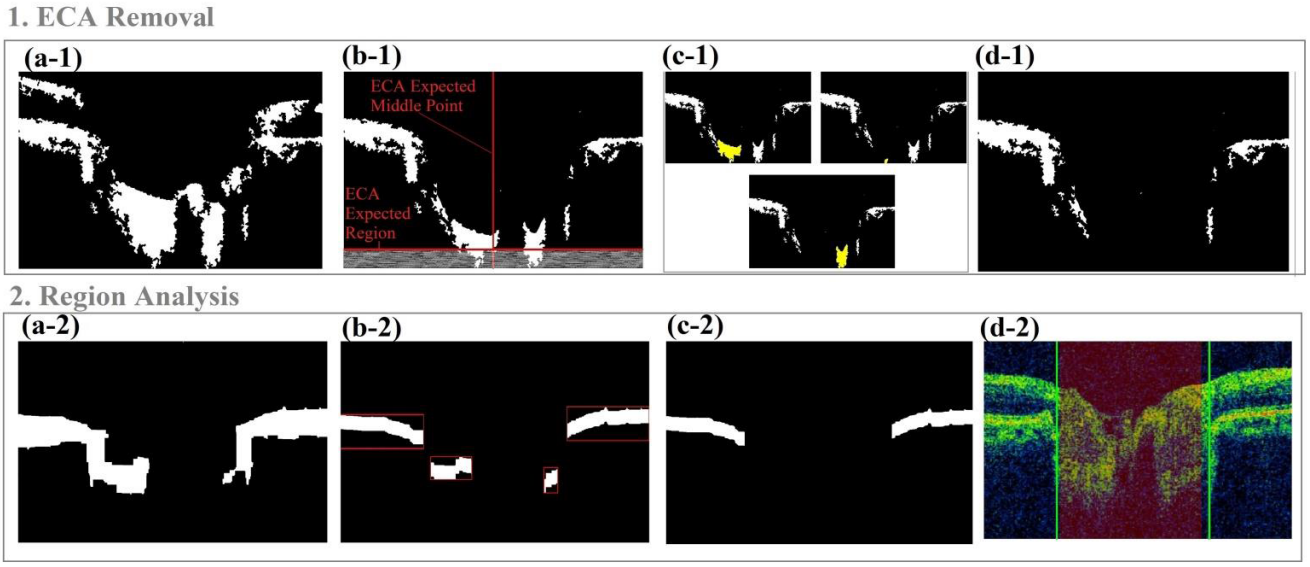

FIGURE 11. ECA Removal & Region Analysis, (a-1) shows resultant binary image 'img' after thresholding, (b-1) shows 'img' after ILM-layer removal. Multiple ECA in ECA expected region can be observed, (c-2) set of images showing identification and removal of ECA in sequence, (d-2) 'img' after removing all ECA, (a-2) another scenario, where undetected ECA is causing RPE-layer extraction error, (b-2) RPE-layer extracted with four portions, (c-2) left & right detected RPE-layer portions, (d-2) accurate disc margin calculation after region analysis.

Figure 11 shows ECA removal. The figure 11 (a-1), which shows a resultant binary image 'img' after the thresholding. Figure 11 (b-1) shows 'img' after the ILM-layer removal. It can be observed that multiple ECA occur in ECA holder defined region and middle point. In figure 11 (c-1), a set of images can be observed. These images demonstrate ECA identification and removal in sequence by using the proposed method. Figure 11 (d-1) shows only the valid RPE portions after removing the multiple ECA.

5) EXTRACTION OF RPE LAYER

There exist only two bottom layers after the removal of all the layers on top of RPE-layer i.e. the RPE-layer and brunch membrane (Figure 10 (d)). The brunch membrane is the lowest retinal layer, whereas, RPE-layer is the second last retinal layer. In order to extract the RPE-layer, the remaining bottom layers have been divided into two folds and top fold is considered as the RPE-layer. The proposed method used for RPE-layer thickness estimation and extraction involves three main steps. In the first step, Top Surface profile (TS_{RPE}) of RPE-layer is calculated by identifying row position of first ON pixel in each column of the processed image 'img'. In the second step, 'img' has been analyzed to calculate the RPE-layer Thicknees-Value (T_V) using TS_{RPE}. Finally, the precise extraction of the RPE-layer from 'img' has been done based on T_V. The T_V has been calculated using following steps.

6) REGION ANALYSIS RPE-LAYER

In few cases, more than two portions of the RPE-layer have been found after the RPE-layer extraction. These multiple portions of the RPE-layer have been generated due to the ECA parts that remained undetected in some rare cases. The region analysis of RPE-layer has been done to detect more than two portions of the RPE layer. The presence of more than two portions indicates some errors in the extraction of the RPE-layer. Therefore, these specific cases have been processed separately. Figures 11 (a-2) show a scenarios where more than two portions of the RPE-layer have been extracted. The 'regionprops' method has been used to calculate the number of RPE-layer-Portions P_{RPE} in processed image 'img' [39]. Figures 11 (b-2) show identified P_{RPE} in red box during region analysis using 'regionprops' method. Each P_{RPE} is then automatically cropped using properties of 'regionprops' method. The size of each cropped P_{RPE} is calculated by counting ON pixels in portion. The two largest portions are selected as valid RPE-layer portions discarding the rest smaller portions as shown in figure 11 (c-2). The accurate RPE-layer termination points detection can be seen in figure 11 (d-2).

7) DETECTION OF LEFT & RIGHT RPE-LAYER END POINTS

The end points of both of the portions have been detected after the extraction of left and right P_{RPE}. These end points have been used to compute cup and disc diameter. The process of end point detection involves two main parts. It starts with detection of Bottom-Surface of RPE-layer (BS_{RPE}) by identifying the first ON pixels at bottom of each column of 'Bimg2'. Then, the Middle-Points of the RPE-layer (MP_{RPE}) have been extracted. Finally, Left RPE-layer End point E_L and Right RPE-layer End point E_R have been calculated from MP_{RPE} by searching first OFF pixel on both sides. Figure 10 (e) shows identified E_L and E_R in the yellow circle.

Algorithm 3 RPE-Layer T_V Calculation

Step 1 START

Step 2 Initialize counter j to zero (Counter to maintain record of calculated thickness values)

Step 3 Initialize thickness counter t to zero (Counter to maintain thickness of each column)

Step 4 For each element in TS_{RPE} (for i = 1 to S, where S is size of TS_{RPE})

Step 5 IF TS_{RPE} (i)! = 0 THEN

- Increase counter j by 1
- Initialize row counter r to zero (Counter to set value of next row to be searched)
- Set Row $\leftarrow TS_{RPE}$ (i) + r
- WHILE (img (Row, i)! = 0) (Keep adding rows till next OFF value occurs)
  - Increase counter r by 1
  - Increase thickness t by 1
  - Set next Row to be searched as Row $\leftarrow TS_{RPE}$ (i) + r
- END WHILE
- Maintain Thickness-profile $T_{RPE} \leftarrow$ (j) t

Step 6 END IF

Step 7 Find Most-Frequently-occurring-value $MF_V \leftarrow$ mode(T_{RPE})

Step 8 Calculated RPE-layer thickness $T_V \leftarrow \frac{MF_V}{2}$

Step 9 STOP

8) CUP AND DISC DIAMETER CALCULATION

Both cup and disc edges have been determined on the basis of the RPE-layer end points. According to studies, the termination points of the RPE-layer are not likely to change substantially with glaucoma progression, and can serve as a stable reference plane [40], [41]. The endpoints of the RPE-layer have been used reliably in clinical practice to define the disc margins on the SD-OCT images [42]. In the proposed system, the distance between the index values of the RPE-layer endpoints has been considered as disc diameter and the end points of the RPE-layer demarcate the margins of the disc. Figure 10 (h) displays disc margins and diameter calculated by considering the RPE-layer end points. The Disc-Diameter D_d has been calculated as following.

$$D_d = R_{index} - L_{index} \tag{1}$$

Likewise, the end points of the RPE-layer have again been used to identify the edges of the cup to compute Cup-Diameter C_d. The cup at a level of the RPE-layer in the SD-OCT images correlates well with clinical reference standards [43]. During our analysis, the mean value of the RPE-layer end points as a reference plane provided better correlation with clinical results to detect the cup edges. The C_d calculation starts with the computation of the mean value of the end points of the RPE-layer. Figure 10 (e) shows a green line representing the mean value of the RPE layer end points. The mean value specifies the location to identify the cup edges on TSimg. Figure 10 (f) shows extracted cup edges shown in the yellow lines on TSimg. Figure 10 (g) shows the detected cup edges and diameter. The C_d has been calculated by taking the difference between C_R and C_L. If no cup edges have been detected in-between end points of the RPE-layer then it has been considered as a flat cup and the sample is considered as healthy. The flat cups have been assigned an absolute value of $C_d = 0$.

IV. CDR CALCULATION

The CDR value has been calculated by taking the percentage of C_d to the D_d as described in equation (2).

$$CDR = C_d/D_d \tag{2}$$

In the case of flat cups, an absolute value CDR = 0.2 has been assigned to the sample.

TABLE 4. AFIO data set summary.

Total Images	Resolution	Healthy	Glaucoma	Image Type
50	951 X 456	22	28	SD-OCT
50	2032 X 1934	22	28	Fundus

V. RESULTS

A. DATA SET DESCRIPTION

A custom dataset acquired from the Armed-Forces-Institute-of-Ophthalmology (AFIO) has been used for the evaluation of the proposed system. The local dataset holds a record of both fundus and SD-OCT images of left and right eyes of the patients. A total of 50 SD-OCT and 50 fundus images of 25 patients (11 Healthy(H) & 14 Glaucoma(G))have been gathered with 951×456 and 2032×1934 resolution, respectively. The dataset has been annotated by four ophthalmologists employed in AFIO. Each patient has been blindly tested by four different ophthalmologists with varying experience. The ophthalmologist 1 is the junior most having least experience whereas; the ophthalmologist 4 is the senior most with maximum experience. To gauge the performance of the proposed system, the computed CDR values using the proposed system have been compared with the CDR values marked by four experts. Table 4 gives a summary of the dataset used for testing. We are going to make it publicly available at www.biomisa.org.

B. RESULTS

Table 5 gives a synopsis of the CDR values annotated by four ophthalmologists (OPT1, OPT2, OPT3 and OPT4). It also provides results of the CDR values computed by means of our proposed methodology for CDR calculation in fundus module using 50 fundus images gathered in the AFIO dataset (FM) [44]. Moreover, it also displays results of the CDR values calculated using the proposed automated OCT module (OM). The performance of the proposed system has been analysed in several ways. Primarily, the results of the proposed system have been correlated with the results of

TABLE 5. Synopsis of CDR calculated values.

Right Eye	OPT1	OPT2	OPT3	OPT4	FM	OM	Left Eye	OPT1	OPT2	OPT3	OPT4	FM	OM
R1	0.3	0.3	0.4	0.3	0.67	0.48	L1	0.3	0.35	0.4	0.5	0.46	0.44
R2	0.6	0.7	0.7	0.75	0.74	0.52	L2	0.5	0.4	0.6	0.7	0.48	0.5
R3	0.8	0.75	0.8	0.7	0.65	0.56	L3	0.3	0.2	0.4	0.5	0.42	0.47
R4	0.3	0.1	0.3	0.2	0.56	0.26	L4	0.3	0.1	0.2	0.2	0.4	0.25
R5	0.3	0.4	0.4	0.4	0.49	0.56	L5	0.3	0.35	0.3	0.4	0.48	0.48
R6	0.6	0.8	0.8	0.7	0.55	0.77	L6	0.5	0.6	0.7	0.7	0.5	0.85
R7	0.3	0.3	0.5	0.5	0.48	0.53	L7	0.5	0.4	0.5	0.45	0.49	0.43
R8	0.6	0.6	0.7	0.7	0.53	0.75	L8	0.5	0.7	0.7	0.7	0.62	0.73
R9	0.3	0.2	0.3	0.4	0.49	0.2	L9	0.8	0.2	0.4	0.3	0.58	0.24
R10	0.5	0.5	0.7	0.6	0.41	0.76	L10	0.6	0.65	0.9	0.6	0.5	0.75
R11	0.9	0.8	0.9	0.9	0.58	0.63	L11	0.3	0.3	0.6	0.2	0.54	0.08
R12	0.4	0.45	0.5	0.6	0.51	0.5	L12	0.5	0.45	0.6	0.5	0.5	0.61
R13	0.3	0.3	0.3	0.4	0.53	0.47	L13	0.8	0.8	0.9	0.9	0.57	0.76
R14	0.5	0.6	0.7	0.7	0.55	0.66	L14	0.6	0.6	0.65	0.6	0.4	0.69
R15	0.2	0.3	0.4	0.25	0.43	0.2	L15	0.3	0.3	0.3	0.2	0.43	0.2
R16	0.3	0.1	0.3	0.3	0.86	0.2	L16	0.3	0.1	0.2	0.4	0.72	0.2
R17	0.4	0.55	0.5	0.6	0.62	0.74	L17	0.5	0.5	0.5	0.5	0.5	0.2
R18	0.4	0.7	0.9	0.7	0.51	0.62	L18	0.3	0.7	0.9	0.65	0.39	0.56
R19	0.65	0.7	0.6	0.7	0.6	0.56	L19	0.6	0.65	0.6	0.7	0.56	0.57
R20	0.4	0.45	0.5	0.5	0.56	0.2	L20	0.75	0.65	0.8	0.9	0.5	0.74
R21	0.6	0.7	0.7	0.8	0.53	0.88	L21	0.6	0.65	0.6	0.8	0.61	0.8
R22	0.8	0.3	0.4	0.4	0.54	0.2	L22	0.4	0.2	0.4	0.4	0.62	0.17
R23	0.3	0.1	0.7	0.3	0.5	0.2	L23	0.7	0.2	0.5	0.3	0.44	0.4
R24	0.6	0.6	0.7	0.7	0.53	0.69	L24	0.5	0.7	0.7	0.75	0.56	0.68
R25	0.2	0.2	0.2	0.3	0.43	0.2	L25	0.3	0.2	0.3	0.3	0.9	0.2

four ophthalmologists. Then, the computed CDR values have been compared with the Computer-Generated-CDR-Values (CGV). Afterwards, the improved performance of the proposed system and suitability of the imaging modality has been demonstrated by comparing it with the fundus CDR values. Finally, the results of the proposed system are compared with the final result of the dataset. The final result has been derived from the results of four ophthalmologists. The sample has been labelled as a normal or glaucomatous on the basis of the majority's decision.

Table 6 shows a set of tables showing the performance of the proposed system with concordance of clinical results annotated by four medical experts. Table 6 (a) shows the performance of the proposed system with the results of OPT1. The system was able to detect 21 out of 26 glaucomatous cases (81% sensitivity) and 18 out of 24 normal cases (75% specificity). Similarly, table 6 (b) shows the outcome of OPT2 results comparison. Results showed that 22 out of 23 glaucomatous cases (96% sensitivity) and 22 out of 27 normal cases were detected accurately (81% specificity).

Likewise, table 6 (c) shows results when system evaluated against OPT3 results. Results showed successful detection of 26 out of 32 glaucomatous cases (81% sensitivity) and 17 out of 18 normal cases (94% specificity).In the same way, the performance of the proposed system as compared with the OPT4 results can be seen in table 6 (d). The system was able to detect 26 out of 30 glaucomatous (87% sensitivity) and 19 out of 20 normal cases (95% specificity).

The performance of the proposed system against the clinical values can also be seen in table 7. It illustrates the

TABLE 6. Results of proposed system compared with clinical results.

Table 6 (a): OPT1 Result

	H	G
H	18	6
G	5	21

Table 6 (b): OPT2 Result

	H	G
H	22	5
G	1	22

Table 6 (c): OPT3 Result

	H	G
H	17	1
G	6	26

Table 6 (d): OPT4 Result

	H	G
H	19	1
G	4	26

TABLE 7. Performance of proposed system with clinical results.

	OPT1	OPT2	OPT3	OPT4
Sensitivity	81%	96%	81%	87%
Specificity	75%	81%	94%	95%
Accuracy	78%	88%	86%	90%

performance measure of the proposed system in term of sensitivity, specificity, and accuracy in comparison with the results of four ophthalmologists. It can be analysed from the table data that our results have shown better correlation with the results of senior ophthalmologist.

The proposed system performance has also been analyzed by comparing the CDR values with CGV. The CGV are automatically calculated during the OCT scan by built-in software Figure 12 shows an error graph between the CGV and CDR

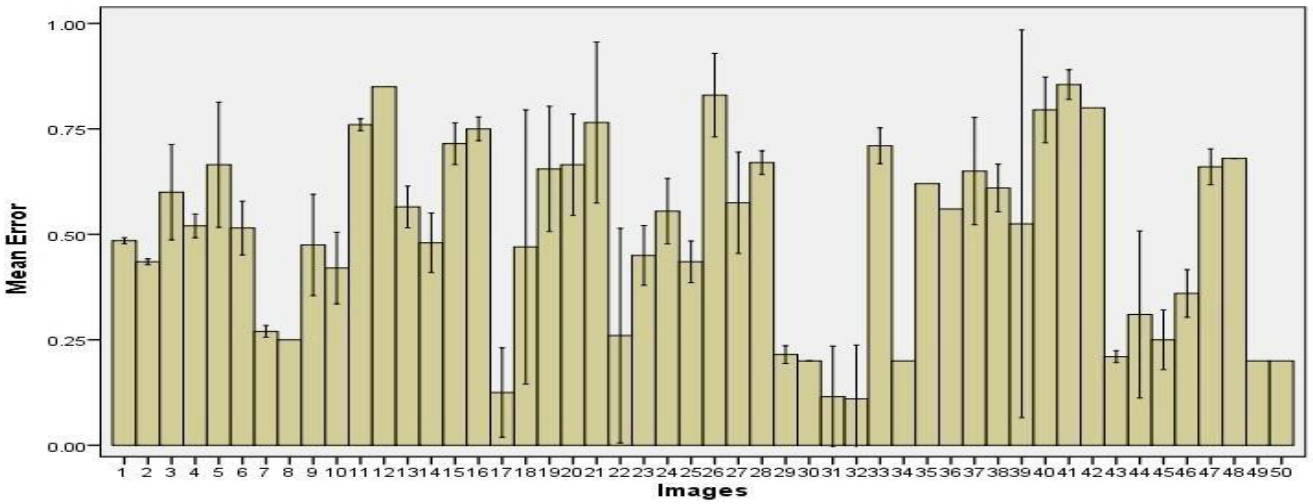

FIGURE 12. CDR value differences between proposed and computer generated values.

values calculated by the proposed system. The lines on the top of each bar indicate the error between the values. It can be observed that in most of the cases error bars show less than 0.15 error in the graph. It proves the similarity of the results of both approaches. Nonetheless, error bars are quite large in some cases. These large bars represent great variations in the results including variation in the class assignment of the sample. Similarly, it can be observed that in some cases there are no error bars. The samples without error bars represent the cases where the built-in software has failed to generate CDR values. According to ophthalmologist in AFIO, the failure in CDR computation occurs due to two main reasons i.e. low visibility of layers and less than 24 B-scan generated during OCT scan. The built-in software needs at least 24 B-Scans to compute CDR values, it usually fails to generate results during examination of patients with blinking problem, children and aged people. Whereas, the proposed system can generate accurate result using a single B-Scan. It can also compute CDR values on less visible layers as compared to built-in software. Therefore, the proposed system has outperformed the results of CGV.

The accuracy of the proposed system computed CDR (OM) values with the CGV and fundus CDR values (FM) can be compared in figure 13. It can be clearly seen that the proposed system has yielded much improved results as compared to the FM and CGV. The fundus images computed CDR values (FM) attained accuracy of 64, 66, 68 and 64 percent with OPT1, OPT2, OPT3 and OPT4 results, respectively.

Similarly, the CGV achieved an accuracy of 76, 78, 80 and 84 percent with OPT1, OPT2, OPT3 and OPT4 results, respectively. Whereas, the proposed system (OM) attained the best performance with accuracy of 78%, 88%, 86% and 90% with OPT1, OPT2, OPT3 and OPT4 results, respectively. These results also elaborate the effectiveness and suitability of the OCT imaging technology for accurate and timely diagnosis of glaucoma. It is quite evident that the proposed method has correctly detected all glaucoma cases

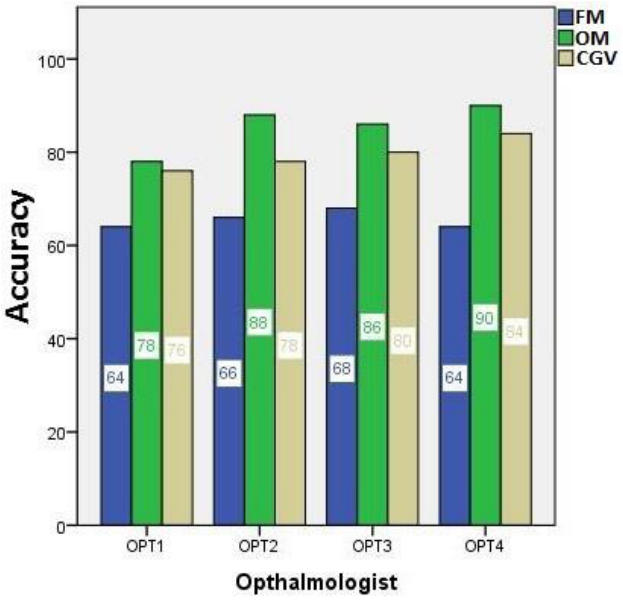

FIGURE 13. Performance comparison of the proposed system with fundus and computer generated diagnosis.

that have been otherwise undiagnosed using the fundus image of the same patient.

Table 8 shows the performance of proposed system with the final result of AFIO data-set. The system showed excellent results by correctly detecting 47 out 50 images, attaining 94% accuracy. It has accomplished 93% sensitivity and 95% specificity. The proposed system has given significantly improved end results as compared to the fundus CDR computation and CGV.

VI. COMPARISON WITH ALREADY DEPLOYED TECHNIQUES

The table 9 displays a feature based comparison of the proposed system with already deployed techniques. It can be observed that the Missing Point (MP) feature has been used

TABLE 8. Performance of proposed system results with final results.

	Healthy	Glaucoma
Healthy	21	1
Glaucoma	2	26

TABLE 9. Comparison of proposed system with already deployed techniques.

	MP	OR	ECA	RA	FC	LQI
CDR computation based on centre of image [20]	NO	NO	NO	NO	NO	NO
CDR computation based on disc edges [19]	NO	NO	YES	NO	NO	NO
CDR calculation using RC boundary [21],	YES	NO	NO	NO	NO	NO
Proposed System	YES	YES	YES	YES	YES	YES

to interpolate missing points by a technique only proposed by Babu *et al.* [21]. In this system, missing points have been predicted by using Bezier curve method. However, the Bezier curve fitting fails to detect outliers in some acute cases and low quality images with a number of consecutive outliers. Similarly, the ECA removal which is very important for accurate layer extraction has been only employed by the method proposed by Wang *et al.* [19]. In this method, the image flattening has been done to remove the extended cup area by removing all the pixels at a distance greater than Q from the ILM layer. This criteria to sense ECA will fail to detect accurate CDR in several cases. Because, in some acute cases, the extended cup areas are at a distance less than the proposed Q distance from the ILM layer. In addition, it can be observed that none of the techniques have catered the issues of outliers, flat cup, RPE layer analysis and low quality images. In this way, an obvious improved performance of our proposed method can be verified by the fact that it has used all the important features including Missing Point (MP), outliers removal (OR), ECA removal, RPE-layer analysis (RA), flat cup (FC) and low quality image (LQI).

VII. DISCUSSIONS

Glaucoma is a silent killer of vision. There are no visible symptoms at an early and treatable stage. Presently, Fundus images are mainly used for the automated diagnosis of glaucoma. These images can only capture structural changes on the outermost layer of the retina. Nevertheless, these indicators appear at the last and untreatable stage. However, structural changes in the internal layers of retina occur prior to VF defects. In this study, automated diagnosis of glaucoma has been carried out by analyzing internal layers of the retina using SD-OCT images taking an average computational time of 10.516 seconds. ILM-layer has been used to identify cup contour. Our unique method to boost ILM layer enabled the system to generate accurate results even with poor visualization. Similarly, our novel TS_{ILM} refinement process generated a solid contour of the cup. This solid contour of cup facilitated the system to calculate cup diameter at exact locations for accurate CDR calculations. Similarly, our new criteria for cup edges determination have remarkably improved the CDR calculation accuracy. The accuracy of CDR value entirely depends on the accuracy of cup diameter calculation. A slight deviation in cup edges can lead to inaccurate results.

The proposed criteria for cup edges determination has given accurate CDR calculation results in both glaucoma and normal cases. Likewise, accurate RPE-layer extraction by considering all rare cases has improved the reliability of the system. The acute cases with ECA are handled effectively increasing the overall accuracy of the system. The ECA defined region helped system to identify and isolate the RPE-layer correctly.

One of the challenging tasks in OCT images is to identify the correct cup in case of multiple curvation on the retinal surface. The proposed system has catered this problem by considering the only curvature that resides between RPE-layer end points. If the system cannot locate cup between RPE-layer end points then the image is considered as normal with the flat cup. Our flat cup standard has enormously improved specificity. The performance evaluation of the proposed system has shown visibly improved results when compared with fundus CDR computed results of the same dataset. The superior performance demonstrated the effectiveness of internal structural changes for the accurate and timely glaucoma diagnosis. Similarly, the feature based comparison with existing techniques shows the power of proposed system for more detailed and comprehensive analysis of retinal layers than its contemporary system. In future, retinal layers can be further analyzed for indicator such as degeneration of ganglion cells. A 3-D generation of RNF-layer for thickness estimation can be an excellent sign to diagnose glaucoma at an early and treatable stage before causing an irreversible damage to OD and vision.

VIII. CONCLUSION

The OCT imaging modality is a modern and sophisticated imaging technology. It can perform comprehensive analysis of retina by scanning the internal layers. The automated glaucoma detection using SD-OCT images is an under researched area and little efforts have been made for the extensive analysis of the retinal layers. In this study, a set of techniques have been proposed for thorough examination of retinal layers to obtain more accurate results. It is important to cater all the acute cases to get a reliable solution. The proposed system has defined several new approaches to successfully deal with the acute cases. It has introduced a new technique to refine the ILM-layer contour to deal with the issues of outliers, measurement errors induced by speckle noise and missing points due to less visible portions of the retinal layers. This method has given significantly improved results as compared to the interpolation and Bezier curve fitting method. Similarly, none of existing system has purvey the problems of outliers, deviations/error on contour of the ILM-layer due to

speckle noise, flat cup, region analysis of the RPE-layer and missing portions due to less visible parts of layers. In this regard, a clear precedence of the proposed systems on its contemporary systems can be seen in terms of accuracy and handling of acute cases. Furthermore, the proposed system has given improved results as compared to CGV due to the ability of handle acute cases and using a single B-scan to generate result. Likewise, satisfactory results have been obtained when evaluation of results have been done with the clinical results. The system has shown excellent results with 94% accuracy when compared with the final results of AFIO dataset. The proposed system correlated more with the results of the senior doctors. Therefore, the proposed system can be used as the decision support system by the young doctors.

ACKNOWLEDGMENT

The authors are extremely thankful to AFIO for providing the dataset as well as grateful to the panel of expert ophthalmologists for annotating the dataset and cross-verifying the results. The research has been carried out under Biomedical Image/Signal Analysis (BIOMISA) research group. www.biomisa.org.

REFERENCES

[1] P. Schacknow and J. Samples, "Glaucoma in the Twenty-First Century," in *The Glaucoma Book*. New York, NY, USA: Springer, 2010, pp. 12–13.

[2] A. F. Clark, "Basic sciences in clinical glaucoma: Steroids, ocular hypertension, and glaucoma," *J. Glaucoma*, vol. 4, no. 5, pp. 354–369, 1995.

[3] B. Nemesure, R. Honkanen, A. Hennis, S. Y. Wu, and M. C. Leske, "Incident open-angle glaucoma and intraocular pressure," *Ophthalmology*, vol. 114, no. 10, pp. 1810–1815, 2007.

[4] F. A. Medeiros and R. N. Weinreb, "Risk assessment in glaucoma and ocular hypertension," *Int. Ophthalmol. Clin.*, vol. 48, no. 4, pp. 1–12, 2008.

[5] P. J. Foster, "The prevalence of glaucoma in Chinese residents of Singapore: A cross-sectional population survey of the Tanjong Pagar district," *Arch. Ophthalmol.*, vol. 118, no. 8, pp. 1105–1111, Jan. 2000.

[6] S. Y. Shen *et al.*, "The prevalence and types of glaucoma in malay people: The Singapore malay eye study," *Investigat. Opthalmol. Vis. Sci.*, vol. 49, no. 9, pp. 3846–3851, Jan. 2008.

[7] "Tunnel vision the economic impact of primary open angle glaucoma—A dynamic economic model," Centre Eye Res. Australia, Univ. Melbourne, Melbourne, VIC, Australia, Tech. Rep., 2008, pp. 80–81.

[8] *Glaucoma Facts and Stats, Glaucoma Research Foundation*. Accessed: Feb. 2017. [Online]. Available: https://www.glaucoma.org/glaucoma/glaucoma-facts-and-stats.php

[9] R. E. Kalina, "Seeing into the future. Vision and aging," *Western J. Med.*, vol. 167, no. 4, pp. 253–257, 1997.

[10] J. Xu *et al.*, "Automated volumetric evaluation of stereoscopic disc photography," *Opt. Exp.*, vol. 18, no. 11, pp. 11347–11359, 2010.

[11] J. S. Schuman *et al.*, "Comparison of optic nerve head measurements obtained by optical coherence tomography and confocal scanning laser ophthalmoscopy," *Amer. J. Ophthalmol.*, vol. 135, no. 4, pp. 504–512, 2003.

[12] J. C. Tsai, MD, New York City. (Jun. 15, 2005). *How to Evaluate the Suspicious Optic Disc, Review of Ophthalmology*. Accessed: May 22, 2017. [Online]. Available: http://www.reviewofophthalmology.com/content/d/cover_focus/i/1315/c/25316/

[13] P. Hrynchak, N. Hutchings, D. Jones, and T. Simpson, "A comparison of cup-to-disc ratio measurement in normal subjects using optical coherence tomography image analysis of the optic nerve head and stereo fundus biomicroscopy," *Ophthalmic Physiol. Opt.*, vol. 24, no. 6, pp. 543–550, 2004.

[14] G. Wollstein, H. Ishikawa, J. Wang, S. A. Beaton, and J. S. Schuman, "Comparison of three optical coherence tomography scanning areas for detection of glaucomatous damage," *Amer. J. Ophthalmol.*, vol. 139, no. 1, pp. 39–43, 2005.

[15] S. Dacosta, S. Bilal, B. Rajendran, and P. Janakiraman, "Optic disc topography of normal Indian eyes: An assessment using optical coherence tomography," *Indian J. Ophthalmol.*, vol. 56, no. 2, pp. 99–102, 2008.

[16] C. K. Leung *et al.*, "Analysis of retinal nerve fiber layer and optic nerve head in glaucoma with different reference plane offsets, using optical coherence tomography," *Investigat. Opthalmol. Vis. Sci.*, vol. 46, no. 3, pp. 891–899, 2005.

[17] H. Y. Shin, H. Y. Park, Y. Jung, J. A. Choi, and C. K. Park, "Glaucoma diagnostic accuracy of optical coherence tomography parameters in early glaucoma with different types of optic disc damage," *Ophthalmology*, vol. 121, no. 10, pp. 1990–1997, 2014.

[18] M. Wu, T. Leng, L. de Sisternes, D. L. Rubin, and Q. Chen, "Automated segmentation of optic disc in SD-OCT images and cup-to-disc ratios quantification by patch searching-based neural canal opening detection," *Opt. Exp.*, vol. 23, no. 24, pp. 31216–31229, 2015.

[19] Y.-P. Wang, Q. Chen, and S.-T. Lu, "Quantitative assessments of cup-to-disk ratios in spectral domain optical coherence tomography images for glaucoma diagnosis," in *Proc. 6th Int. Conf. Biomed. Eng. Inform.*, Dec. 2013, pp. 160–165.

[20] R. Nithya and N. Venkateswaran, "Analysis of segmentation algorithms in colour fundus and OCT images for glaucoma detection," *Indian J. Sci. Technol.*, vol. 8, p. 24, Jan. 2015.

[21] T. R. G. Babu, S. S. Devi, and R. Venkatesh, "Optic nerve head segmentation using fundus images and optical coherence tomography images for glaucoma detection," *Biomed. Papers*, vol. 159, no. 4, pp. 607–615, 2015.

[22] T. R. G. Babu, S. Devi, and R. Venkatesh, "Automatic detection of glaucoma using optical coherence tomography image," *J. Appl. Sci.*, vol. 12, no. 20, pp. 2128–2138, 2012.

[23] *MathWorks: Crop an Image*. Accessed: Feb. 2017. [Online]. Available: http://www.mathworks.com/help/images/ref/imcrop.html

[24] P. Bhatt, S. Patel, A. Shah, and S. Patel, "Image enhancement using various interpolation methods," *Int. J. Comput. Sci. Inf. Technol. Secur.*, vol. 2, no. 4, pp. 799–803, Aug. 2012.

[25] P.-S. Liao, T.-S. Chen, and P.-C. Chung, "A fast algorithm for multilevel thresholding," *J. Inf. Sci. Eng.*, vol. 17, no. 5, pp. 713–727, 2001.

[26] A. Ozcan, A. Bilenca, A. E. Desjardins, B. E. Bouma, and G. J. Tearney, "Speckle reduction in optical coherence tomography images using digital filtering," *J. Opt. Soc. Amer. A, Opt. Image Sci.*, vol. 24, no. 7, pp. 1901–1910, 2007.

[27] *2-D Adaptive Noise-Removal Filtering—MATLAB Wiener2*. Accessed: May 2017. [Online]. Available: https://www.mathworks.com/help/images/ref/wiener2.html

[28] *Convert Matrix to Grayscale Image—MATLAB Mat2gray*, Mathworks.com. Accessed: Feb. 2017. [Online]. Available: https://www.mathworks.com/help/images/ref/mat2gray.html?requestedDomain=true

[29] (2017). *Adjust Image Intensity Values or Colormap—MATLAB Imadjust–MathWorks United Kingdom. Mathworks.com*. Accessed: May 2017. [Online]. Available: https://www.mathworks.com/help/images/ref/imadjust.html

[30] *Maths Works Bwareaopen*. Accessed: Feb. 2016. [Online]. Available: http://www.mathworks.com/help/images/ref/bwareaopen.html

[31] *Morphological Image Processing*. Accessed: May 2017. [Online]. Available: https://www.cs.auckland.ac.nz/courses/compsci773s1c/lectures/ImageProcessing-html/topic4.htm

[32] *BWselect, Fill Image Regions and Holes—MATLAB Imfill*. Accessed: May 2017. [Online]. Available: https://www.mathworks.com/help/images/ref/imfill.html

[33] *Ind2Sub, Find Indices and Values of Nonzero Elements*. Accessed: May 2017. [Online]. Available: https://www.mathworks.com/help/matlab/ref/find.html

[34] (Jun. 6, 2016). *How to Identify Outliers in Your Data, Machine Learning Mastery*. Accessed: May 22, 2017. [Online]. Available: http://machinelearningmastery.com/how-to-identify-outliers-in-your-data/

[35] J. Fisher, J. Lowther, and C.-K. Shene, "Curve and surface interpolation and approximation: Knowledge unit and software tool," *ACM SIGCSE Bull.*, vol. 36, no. 3, pp. 146–150, 2004.

[36] A. M. Bagci, M. Shahidi, R. Ansari, M. Blair, N. P. Blair, and R. Zelkha, "Thickness profiles of retinal layers by optical coherence tomography image segmentation," *Amer. J. Ophthalmol.*, vol. 146, no. 5, pp. 679–687, 2008.

[37] M. Dalla Mura, J. A. Benediktsson, B. Waske, and L. Bruzzone, "Morphological attribute profiles for the analysis of very high resolution images," *IEEE Trans. Geosci. Remote Sens.*, vol. 48, no. 10, pp. 3747–3762, Oct. 2010.
[38] M. Boldt, K. Schulz, A. Thiele, and S. Hinz, "using morphological differential attribute profiles for change categorization in high resolution SAR images," in *Proc. Int. Arch. Photogramm., Remote Sens. Spatial Inf. Sci. (ISPRS)*, vol. 11. 2013, pp. 29–34.
[39] *Measure Properties of Image Regions—MATLAB Regionprops*. Accessed: May 2017. [Online]. Available: https://www.mathworks.com/help/images/ref/regionprops.html
[40] N. G. Strouthidis *et al.*, "Comparison of clinical and spectral domain optical coherence tomography optic disc margin anatomy," *Investigat. Opthalmol. Vis. Sci.*, vol. 50, no. 10, pp. 4709–4718, 2009.
[41] N. G. Strouthidis, H. Yang, B. Fortune, J. C. Downs, and C. F. Burgoyne, "Detection of optic nerve head neural canal opening within histomorphometric and spectral domain optical coherence tomography data sets," *Investigat. Opthalmol. Vis. Sci.*, vol. 50, no. 1, pp. 214–223, 2009.
[42] S. M. Iverson and M. Sehi, "The comparison of manual vs automated disc margin delineation using spectral-domain optical coherence tomography," *Eye*, vol. 27, no. 10, pp. 1180–1187, 2013.
[43] Z. Hu, M. D. Abràmoff, Y. H. Kwon, K. Lee, and M. K. Garvin, "Automated segmentation of neural canal opening and optic cup in 3D spectral optical coherence tomography volumes of the optic nerve head," *Investigat. Opthalmol. Vis. Sci.*, vol. 51, no. 11, pp. 5708–5717, 2010.
[44] T. Khalil, M. U. Akram, A. Jameel, and S. Khalid, "Improved automated detection of glaucoma from fundus image using hybrid structural and textural features," *IET Image Process.*, vol. 11, no. 9, pp. 693–700, 2017, doi: 10.1049/iet-ipr.2016.0812.

TEHMINA KHALIL was born in Islamabad, Pakistan, in 1982. She received the B.S. degree (Hons.) in computer science from the University of Azad Jammu and Kashmir, Mirpur, Pakistan, in 2006, and the M.S. degree in software engineering from Bahria University, Islamabad, Pakistan, in 2009. She is currently pursuing the Ph.D. degree with Bahria University. She was a Programmer at LMKR, Islamabad. She is currently a Lecturer with the Mirpur University of Science and Technology, Mirpur. Her main areas of research are biomedical imaging and image processing.

M. USMAN AKRAM was born in Islamabad, Pakistan, in 1985. He received the B.S. degree (Hons.) in computer system engineering and the master's and Ph.D. degrees in computer engineering from E&ME (NUST), Rawalpindi, Pakistan, in 2008, 2010, and 2012, respectively. He is currently an Assistant Professor with E&ME (NUST). His main areas of research are biomedical imaging and image processing.

HINA RAJA is currently the Ph.D. Scholar with the Computer Engineering Department, E&ME (NUST), Rawalpindi, Pakistan. Her main areas of research are image processing and machine learning.

AMINA JAMEEL was born in Islamabad, Pakistan, in 1982. She received the B.E. degree (Hons.) in electrical (telecom) engineering and the Ph.D. degree in electrical engineering from MCS (NUST), Rawalpindi, Pakistan, in 2005 and 2014, respectively. She is currently an Associate Professor with Bahria University, Islamabad, Pakistan. Her main areas of research are image and signal processing.

IMRAN BASIT is a Senior Consultant and an Opthalmologist. He is currently with the Armed Forecs Insititute of Opthalmology.